

Prepared for the National Institutes of Health
National Institute of Neurological Disorders and Stroke
Division of Stroke, Trauma and Neurodegenerative Disorders
Neural Prosthesis Program
Bethesda, MD 20892

Microstimulation of the Lumbosacral Spinal Cord: Mapping

NIH-NINDS-NO1-NS-8-2300

Quarterly Progress Report #6

Period Covered: 1 January, 2000 - 31 March, 2000

Principal Investigator: Warren M. Grill, Ph.D.

Co-Investigators: Kenneth J. Gustafson, Ph.D.
Musa A. Haxiu, M.D., Ph.D.
Michel A. Lemay, Ph.D.

Department of Biomedical Engineering
Case Western Reserve University
Cleveland, OH 44106-4912

ABSTRACT

The objectives of this research are to determine the anatomical locations of spinal neurons involved in control of the genitourinary and hindlimb motor systems, and to determine the physiological responses evoked in the genitourinary and hindlimb motor systems by intraspinal microstimulation. During this quarter we made progress toward both of these objectives. We were successful in using immunocytochemistry to identify sacral spinal neurons that express the inhibitory neurotransmitter glycine. Secondly, we completed development of the software interface for our 2 degree-of-freedom cartesian robot to characterize the hindlimb motor responses evoked by microstimulation of the lumbar spinal cord. Thirdly, we continued development of a technique to use recordings of potential on the surface of the spinal cord to localize active neurons within the spinal gray matter.

INTRODUCTION

Electrical stimulation of the nervous system is a means to restore function to individuals with neurological disorders. The objective of this project is to investigate the feasibility of neural prosthetics based on microstimulation of the spinal cord with penetrating electrodes. Specifically, chemical and viral retrograde tracers, immediate early gene expression, and immunocytochemistry are used to determine the locations and neurochemical identity of neurons in the spinal cord that control genitourinary and motor functions in the male cat. Microstimulation with penetrating activated iridium microelectrodes is used to determine the physiological effects in the genitourinary and motor systems of activation of different neural populations. Finally, inverse potential mapping is being explored as a method to determine, via spinal surface potential recordings, the location of active populations of neurons. The results of this project will provide data important to understanding neural control of genitourinary and motor functions, answer fundamental questions about microstimulation of the spinal cord, and lead to development of a new generation of neural prosthetics for individuals with neurological impairments.

PROGRESS IN THIS QUARTER

During the sixth quarter of this contract we continued a series of experiments using immunocytochemistry to identify sacral spinal neurons containing the inhibitory

neurotransmitter glycine. We also completed development of a software interface to control and run experiments with our 2 degree-of-freedom cartesian robot that will be used to measure the hindlimb motor responses evoked by microstimulation of the lumbar spinal cord. Thirdly, we continued development of an inverse technique to map locations of active spinal neurons using potential recordings on the surface of the spinal cord. Below each of our accomplishments is summarized.

Identification of Glycinergic Sacral Spinal Neurons

During reflex micturition the motoneurons innervating the external urethral sphincter are synaptically inhibited and pudendal afferent fibers receive presynaptic inhibition. The objective of these experiments is to identify inhibitory neurons that are active during reflex micturition. We have previously used patterns of c-Fos, the protein product of the immediate early gene c-fos, to identify spinal neurons active during reflex micturition in the male cat [Grill et al., 1998a], and used co-localization of c-Fos and parvalbumin [Grill et al., 1998b] and co-localization of the neurotransmitter gamma-amino butyric acid (GABA) to identify putative inhibitory neurons that are active during reflex micturition [QPR#1, NIH-NINDS-NO1-NS-8-2300].

The present experiments are designed to identify glycinergic neurons that are active during reflex micturition by co-localization of c-Fos and glycine. As described in the last QPR, we tried a large number of combinations of antibodies and dilution we did not obtain reliable labeling of glycine in spinal neurons. We did see occasionally labeled neurons as well as labeled fibers, but the intensity and repeatability of labeling was unsatisfactory.

It has been established that fixatives containing aldehyde can mask antigens (e.g., glycine) by protein crosslinking and/or protein denaturation [Fox et al., 1985, Dapson, 1993] or by complexing of hydromethyl groups between neighboring proteins [Morgan et al., 1997]. As this tissue was fixed with paraformaldehyde this may explain the poor labeling that we observed. In the current quarter we tested heating and calcium chelation to recover glycine antigenicity [Jiao et al., 1999] and successfully demonstrated immunochemical detection of glycine in cat spinal neurons.

METHODS

Immunocytochemistry was used to detect the presence of glycine in neurons in the lumbosacral spinal cord of cats. All animal care and experimental procedures were according to NIH guidelines and were reviewed and approved by the Institutional Animal Care and Use Committee of Case Western Reserve University. The details of the experimental preparation can be found in Grill et al. [1998]. The animals were perfused via the aorta with saline followed by 4% paraformaldehyde in 0.1M NaPO₄ (pH=7.4).

The brain and spinal cord were removed, stored in fixative for 2-5 days, and then transferred to 30% sucrose in 0.1M NaPO₄ (PBS) for 2-4 days. Tissue from these preliminary studies was taken from the lumbar segments, rather than from the sacral segments which are ultimately of interest.

The sacral spinal cord was sectioned transversely at 50 µm intervals on a freezing microtome and a 1 in 5 series of sections were processed for immunocytochemical detection of glycine. In contrast to our previous efforts, sections were put through an antigen retrieval step prior to immunocytochemical processing. Floating sections were incubated for 30 min in 30 mM sodium citrate at 80°C [Jiao et al., 1999]. Floating sections were rinsed in phosphate buffered saline (PBS), rinsed in PBS containing 0.3% Triton X-100 for 1 h, and then exposed to primary antibody against glycine (mouse anti-glycine, Alpha Diagnostics) 1:100 in a blocking solution of PBS/Triton/BSA 1% overnight on a shaker at 4 degrees. Sections were then washed in PBS/Triton 3X for 5 minutes. Next, the sections were exposed to an appropriate biotinylated goat anti-mouse secondary antibody (Jackson Labs) 1:200 in a blocking solution of PBS/Triton/BSA for 1-4 hrs at room temperature. Sections were washed with PBS 2X for 10 minutes and processed using a standard biotin avidin peroxidase kit (ABC Elite, Vector Laboratories, Burlingame, CA) at 5µl/ml in PBS for 1hr at room temperature. Sections were washed in PBS 3X for 5 minutes and placed in a DAB solution (Sigma) with nickel chloride enhancement for 30-90 seconds. Sections were then washed 2X in ddH₂O for 5 minutes and 1X in PBS, mounted on gelatin coated slides, air dried, dehydrated in ascending concentrations of alcohol from 70%-100%, coverslipped with Paramount mounting medium and viewed with a light microscope.

RESULTS AND DISCUSSION

The antigen retrieval step resulted in robust immunocytochemical detection of glycine in the cat lumbosacral spinal cord. Figure 6.1 illustrates examples of spinal cord sections from the same animal that were processed without (A, B) and with (C,D) the antigen retrieval step. In the former case, there is no evidence of glycine antigenicity, while in the later case there are neurons clearly exhibiting glycine antigenicity as seen by the reaction product in the cytoplasm in combination with clear nuclei.

It has been established that fixatives containing aldehyde can mask antigens, and this appears to explain the poor labeling that we observed in our previous studies. Heating and calcium chelation clearly improved glycine antigenicity, and resulted in robust labeling of neurons in the cat lumbosacral spinal cord. In the next quarter we will combine glycine immunochemistry with immunochemical detection of c-Fos to identify glycinergic neurons that were active during reflex micturition.

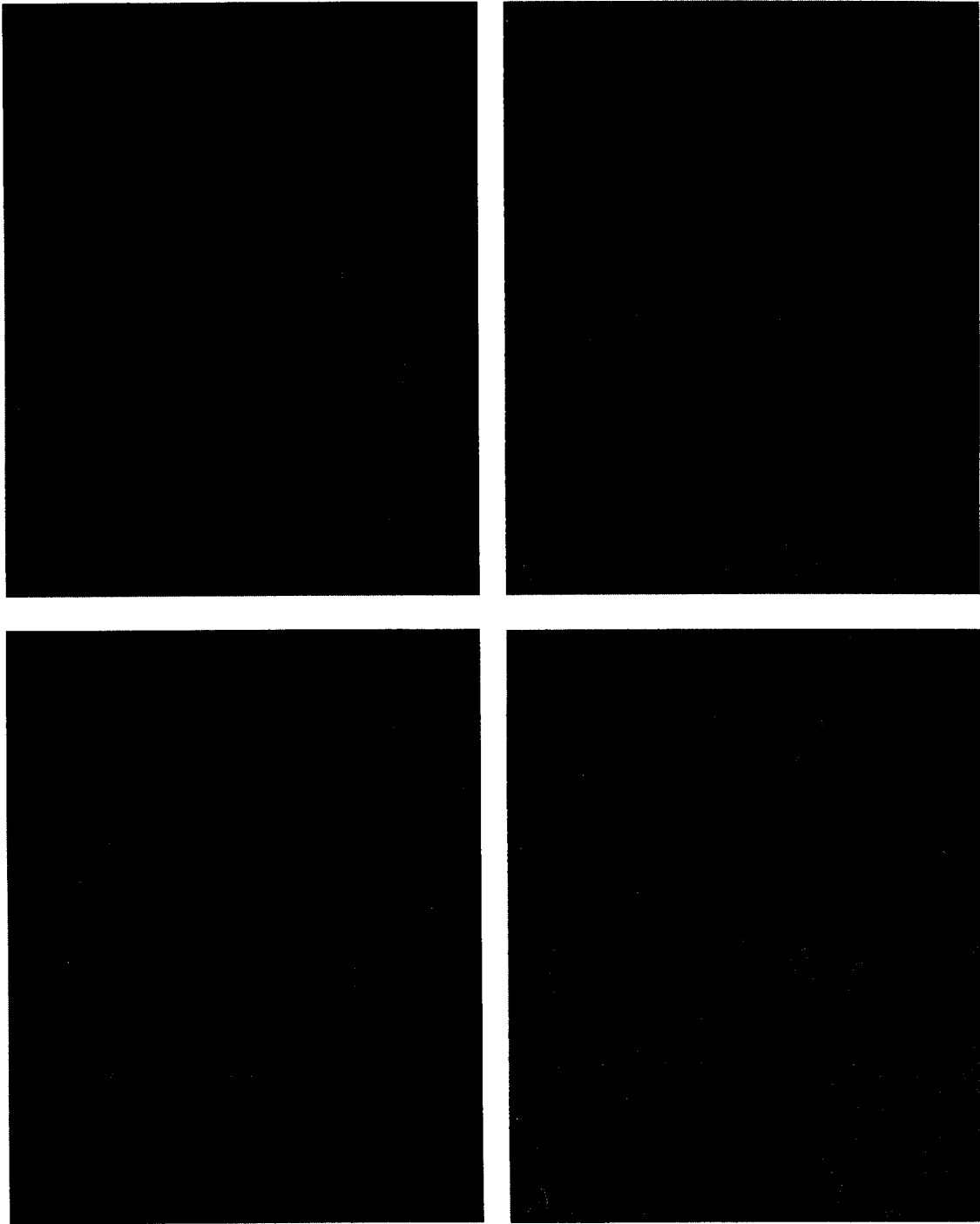


Figure 6.1 Immunocytochemical detection of glycine in cat lumbosacral spinal cord. Photomicrographs of section of the lumbosacral spinal cord showing the absence of glycinergic labelling when no antigen retrieval step was used (A,B), and robust labeling of glycine following an antigen retrieval step (heating and calcium chelation) applied prior to immunochemical processing.

Development of a User Interface to the Planar Manipulator for the Characterization of Feline Hindlimb Mechanical Properties

Our on-going investigations of the cat hindlimb response to intraspinal microstimulation have revealed that patterns of forces, termed force fields, are produced when electrical stimulation is applied to the spinal cord of the animal. The force fields are of a set of vectors, each plotted at the limb position at which it was measured, with vector length proportional to force magnitude and vector direction representing force orientation. Thus far our measurements have been made under isometric conditions. To expand our investigation to movement conditions, we designed and assembled a two degree-of-freedom robot described in QPR#5. The robot is intended to measure the mechanical properties of the cat hindlimb in the sagittal plane, and was designed to provide two primary functions: the ability to record the movement produced by the force field, and the ability to impose controlled forces to the limb while simultaneously recording the resulting movement and reaction forces. In this quarter we developed a computer interface to control the robot during experiments designed to measure the isometric forces produced by intraspinal stimulation, and the motion produced by the spinal force field.

Robotic System Architecture

A diagram of the overall system is depicted in Figure 6.2. The manipulandum is a parallelogram mechanism which allows direct drive of each joint. One motor controls the inner or shoulder joint, while the other motor controls the outer or elbow joint. The shafts' rotary positions are sensed via encoders, and a six-axis force sensor measures the forces applied on the end-point (to which the cat's paw will be attached). The position and force information are stored/processed by a computer that also produces the desired motor command. Power is supplied to the motors via two power amplifiers that convert the computer command voltage to a controlled current.

Robot Software Architecture

The robot control system is based on sensing information from the robot, either end-point force or position, and updating the current applied to the motors to obtain the desired end-point behavior. Since the sensing/updating is critically dependent on time, the control interface was developed in the C programming language running under a real-time operating system (QNX Software Systems Ltd.). Interrupt latency is minimal (3.3 μ sec on a 166 MHz Pentium, our system is a 450 MHz Pentium), allowing sampling rates of about 2000 Hz. The structure of the control interface is given in figure 6.3. The data acquisition card (see figure 6.2) is set to generate interrupts at the desired sampling rate (acquisition is in burst mode, i.e. channels are sampled consecutively at the card's

maximal rate ≈ 333 KHz). Once the card is set, the program goes into an interrupt waiting mode and the encoders (position) and sampled channels are read upon receipt of the interrupt. The desired motor currents are then calculated, and the command to the current amplifiers is output on the card's analog outputs. The program then saves the current sensor information, and waits for the next interrupt. Since the robot controller is programmed in software, a variety of control laws can be implemented easily. A combination of two control laws are used for a typical experiment. The first one is a simple stiffness controller that makes the robot behave as a two-dimensional spring by relating restoring force to displacement ($\mathbf{F}=\mathbf{K}\times\Delta\mathbf{X}$). The second controller activates the motors to compensate for the effects of gravity. The robot thus appears to be mass-less, and is easily driven by the cat's hindleg during motion experiments.

User Interface Implementation

The user interface consists of a series of menus that allow the user to 1) select the locations for the isometric force measurements, 2) select the stimulation parameters to be delivered, 3) collect forces with the robot holding the paw at the selected locations, and 4) measure the movement produced by the stimulation level chosen. Each trial is collected by calling the basic structure described in Figure 6.3. The stimulation parameters, controller to be used (stiffness or gravity compensation), and file information are all passed to the main robot control routine. The robot is de-activated between trials, allowing the user to make adjustments to parameters between trials.

The data collected is examined between trials using gnuplot, a freeware plotting package widely used in the Unix community. Each of the saved channels is displayed, and the user can plot a force field of the files specified and in the time range desired. The visual and basic data statistics can then be used to adjust the stimulation level and/or the locations at which forces are measured.

ROBOTIC SYSTEM DIAGRAM

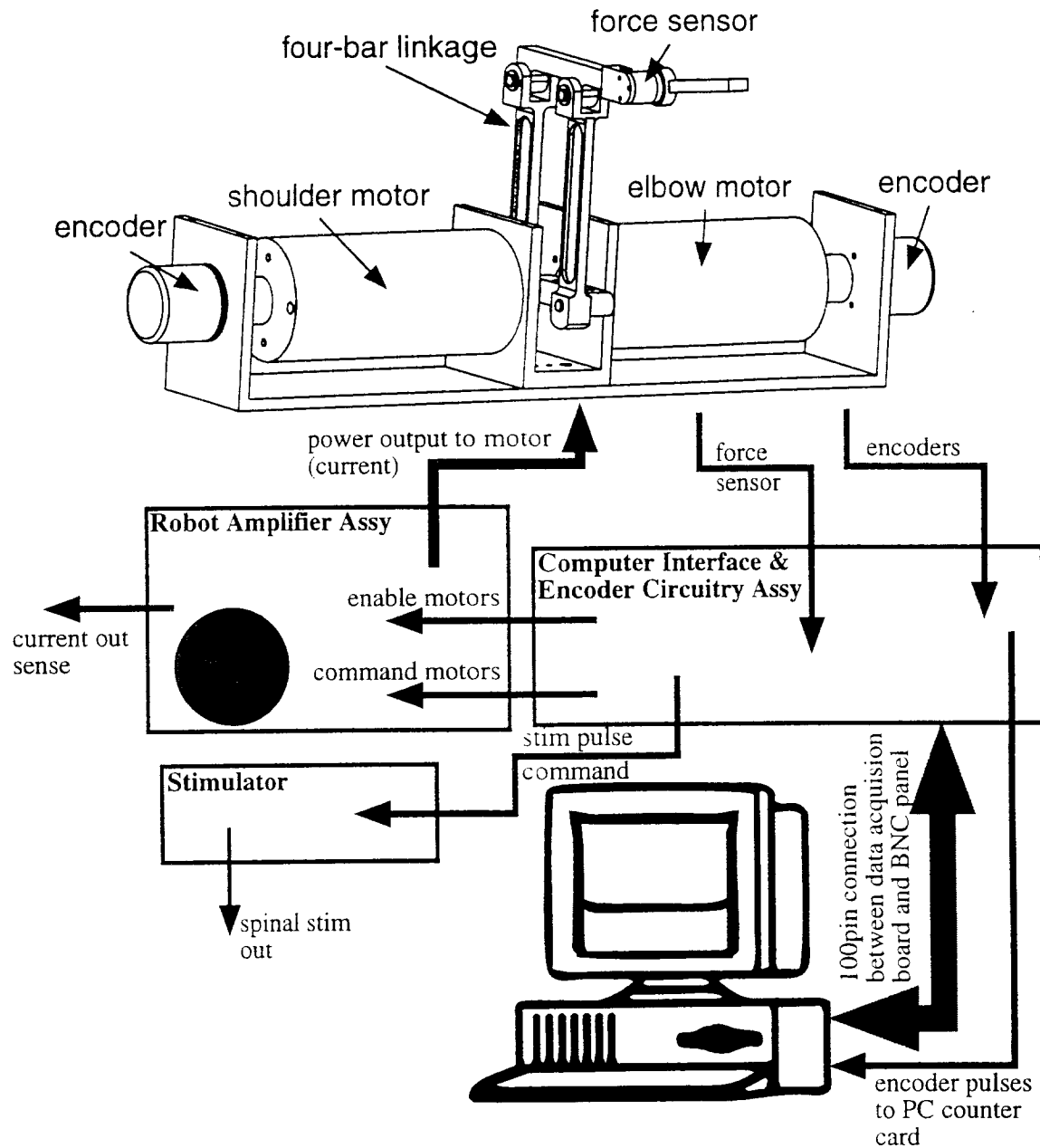


Figure 6.2 Diagram of the overall two degree-of-freedom planar robot system. The kinematic linkage and motor assembly are shown at the top. Robot movement is in the vertical plane, which corresponds to the animal's sagittal plane. Position is sensed by optical encoders attached to the motors' rear shaft. End-point force is sensed by a commercial six-axis force transducer mounted at the end of the outer linkage. A gimball, to which the paw is attached, is mounted on the force transducer, and allows the rotation of the ankle joint that occurs as the limb is moved. Outside information is passed to and from the PC data acquisition board (DAQ) via the Computer Interface & Encoder Circuitry Assembly. The encoder signal is the only information that is not processed by the DAQ, and is instead fed into a counter card mounted inside the computer. Digital to analog outputs from the DAQ board are used to control amplifiers supplying current to the motors (Robot Amplifier Assembly). Three counters on the DAQ board are used to generate a TTL pulse train that drives a current controlled stimulator.

Robotic Software Main Routine

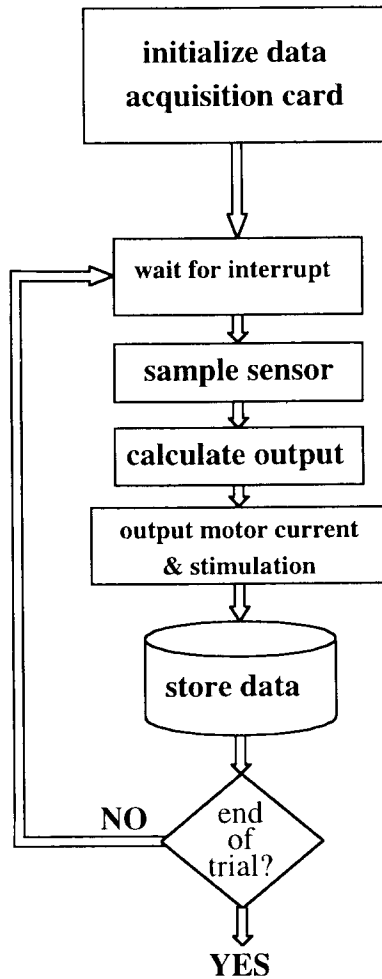


Figure 6.3. Flow chart of the robot control software main routine. Once the data acquisition card is initialized the program waits for an interrupt. Upon interrupt, the DA channels are sampled along with the encoder counter card. This provides the control software the information necessary to calculate the motor currents necessary to implement the desired robot end-point behavior. The desired currents are output as voltages to the current amplifiers. The data is then stored, and the end-of-trial condition is verified. If finished, then the routine terminates, if not, then the routine waits for the next interrupt.

Development of an Intraoperative Spinal Cord Mapping Procedure

IMPLEMENTATION OF THE THIRD FORWARD MODEL

In QPR 4 we reported on the development of 2 forward models. During this quarter we implemented a third forward that included anisotropy in the white matter region. The third forward model is geometrically identical to the second model, but as shown in figure 6.4, anisotropy was incorporated into the electrical properties of the outer cylindrical region to better represent the properties of the white matter [Ranck and BeMent, 1965]. As in the first and second models, the electrical properties of the inner cylindrical region and the bath are homogenous and isotropic. There are two important aspects of the three model outputs that were compared and contrasted. First the shape, or profile, of the surface potential fields generated by each model was examined. Second, differences in the magnitudes of the three model outputs were analyzed. Subsequently, we conducted a sensitivity analysis that demonstrates that the model output is indeed sensitive to the location of the current source within the inner cylinder.

Influence of model electrical properties on surface potentials

To compare the shapes of potential fields without bias due to the magnitude differences, outputs were normalized by dividing the solution at every point by the peak value of the solution matrix. The normalized surface potential maps are shown in figure 6.5. These contour maps are generated from the solution matrix. They show the solution for a 4cm range in z (2 cm rostral and caudal to the source) and π radians range in θ , or half of the cylinder. Recall that the source location in the θ and z -dimensions is defined to be zero, thus the peak potential for each map is found at these coordinates. As expected, the potential was seen to decay at locations further from the source in both the θ and z -directions. There are noticeable surface potential differences induced by inhomogeneity of the outer cylinder (middle map of fig. 6.5), and even more by anisotropy (bottom map of fig. 6.5). Note that each succeeding output has fewer contours for the same range in the z -direction; this “spreading” of the potential in z is particularly evident in the anisotropic case. A similar spreading in the θ -direction also occurred, but it was a much smaller effect.

Difference maps were constructed to quantify the effects of the inhomogeneity and anisotropy. The top map of figure 6.6 shows the difference between the normalized potentials generated by the first and second forward models, intending to highlight the effects of inhomogeneity on the voltage profile. We see that the addition of the outer cylindrical region of model two primarily affects the shape of the solution in the z -direction, and that the shape difference is about 2% at $z = 2$ cm. The bottom map of figure 6.6 shows the difference between the normalized potentials generated by the second and third forward, emphasizing the effect of anisotropy in the outer cylindrical region on the voltage profile. Anisotropy induces an even greater shape change in the z -

direction, an additional 2.8%. The bottom map also shows that anisotropy induces a shape change in the θ -direction at some z levels rostral and caudal to the source.

Differences in the profile of the surface potentials can also be seen by comparing the solution at specific lines along the surface of the cylinder. The potential along two lines, $z = 0$ and $\theta = 0$, are shown in fig. 6.7. Shape differences are quite noticeable in the z -direction, where the sharpness near the source in the first model became smoother in each succeeding model. Similar shape differences to a smaller degree were observed in the θ -direction at $z = 0$. Figure 6.7 also shows magnitude differences between each of the three models. A decline in the peak magnitude resulted from both the addition of inhomogeneity (10%) and anisotropy (an additional 13%).

Effect of source location on surface potentials

For our mapping approach to be successful, it is necessary that information about the location of the source be available in the surface potentials. The results showed that the voltage profile, particularly the profile near the source, was affected by changes in the source location.

Simulations using the third forward model were run with the values listed in Table 1, and changes were made only to the source location. A parameter named DIF was used to perform the analyses and monitor change. DIF is defined as the difference in maximum and minimum voltage values along some specified region of the model solution (fig. 6.8). Following each simulation, the data were normalized by division of the peak voltage value, and three DIF values were recorded: the magnitude of the voltage ranges along $\theta = 0$ for $-2\text{cm} \leq z \leq 2\text{cm}$, along $\theta = \pi$ for $-2\text{cm} \leq z \leq 2\text{cm}$, and along $z = 0$ for $-\pi \leq \theta \leq \pi$. The peak voltage of the output matrix before normalization was also recorded. The source location was changed both in the ρ -direction and in the θ -direction. In the ρ -direction, the source was moved from the center of the cylinder ($b = 0$) in 0.5mm increments to the edge of the gray matter region ($b = 2.5\text{mm}$). In the θ -direction, the source was moved from one side of the cylinder ($\theta = 0$ rad) to the other ($\theta = \pi$ rad) in increments of $\pi/4$ radians.

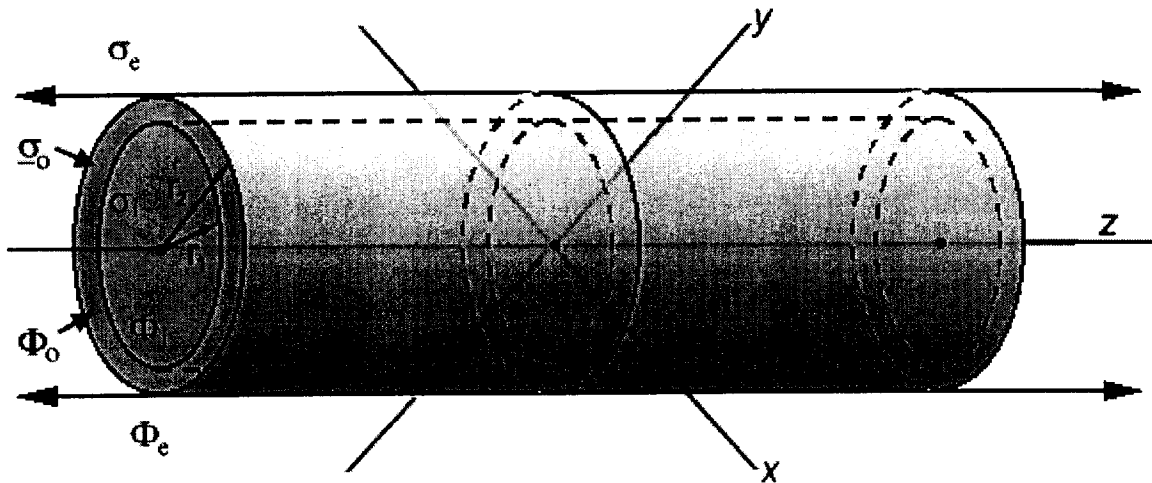
The effect of the source location on the distribution (DIF) and magnitude of the surface potentials is shown in figure 6.9. As the source was moved from the center toward the surface of the cylinder, $\text{DIF}_{z,\text{near}}$ became larger (~6% change in voltage profile), and $\text{DIF}_{z,\text{far}}$ became smaller (~2% change in voltage profile). Also noticeable, was a substantial change in the parameter $\text{DIF}_{\theta,\text{near}}$ (~8% change in voltage profile). $\text{DIF}_{\theta,\text{near}}$ was found to be more sensitive to changes in the parameter b than to changes in any other parameter. Interestingly, the peak magnitude was found to be quite insensitive

to source location changes in the ρ -direction, going from 50.1mV at $b=0\text{mm}$ to 53.9mV at $b=2.5\text{mm}$.

For any source location changes in the θ -direction, DIF_θ will remain the same and is not shown. As the source is moved from $\theta = 0$ to $\theta = \pi$, both $\text{DIF}_{z,\text{near}}$ and $\text{DIF}_{z,\text{far}}$ change substantially ($\sim 5\%$ change in voltage profile), $\text{DIF}_{z,\text{near}}$ decreasing and $\text{DIF}_{z,\text{far}}$ increasing by that same amount. The peak magnitude is, by symmetry, insensitive to θ -direction changes in the source location.

CONCLUSION

We have developed and implemented a series of models of the potential generated on the surface of the spinal cord by intraspinal current sources. In this quarter we implemented a third forward model that included white matter anisotropy. Anisotropy was found to have a substantial effect on the shape and magnitude of the surface potentials. We also analyzed the effect of source location on surface potentials and demonstrated that source location information is projected to the surface of the cylinder in the surface potential profile and magnitude.



Parameter	Description
r	Cylinder radius
σ_i	Conductivity of cylindrical region
σ_e	Conductivity of outside the cylinder
Φ_i	Scalar potential field inside the cylinder
Φ_e	Scalar potential field outside the cylinder
I	Monopolar source; always located at $(b,0,0)$

Model	Annulus Conductivity (σ_o)
2 nd	$\sigma_o = \sigma_o$ (isotropic)
3 rd	$\sigma_o = \sigma_z + \sigma_t$ (anisotropic \otimes longitudinal and transverse components)

FIGURE 6.4: The second and third forward models are illustrated above. Both models are composed of concentric cylinders of radii r_1 and r_2 , as seen in the figure. The difference in the two models is found in the electrical properties of the outer cylindrical or annulus region; while this region is isotropic in the second forward model, it is anisotropic in the third, as noted in the lower of the tables above.

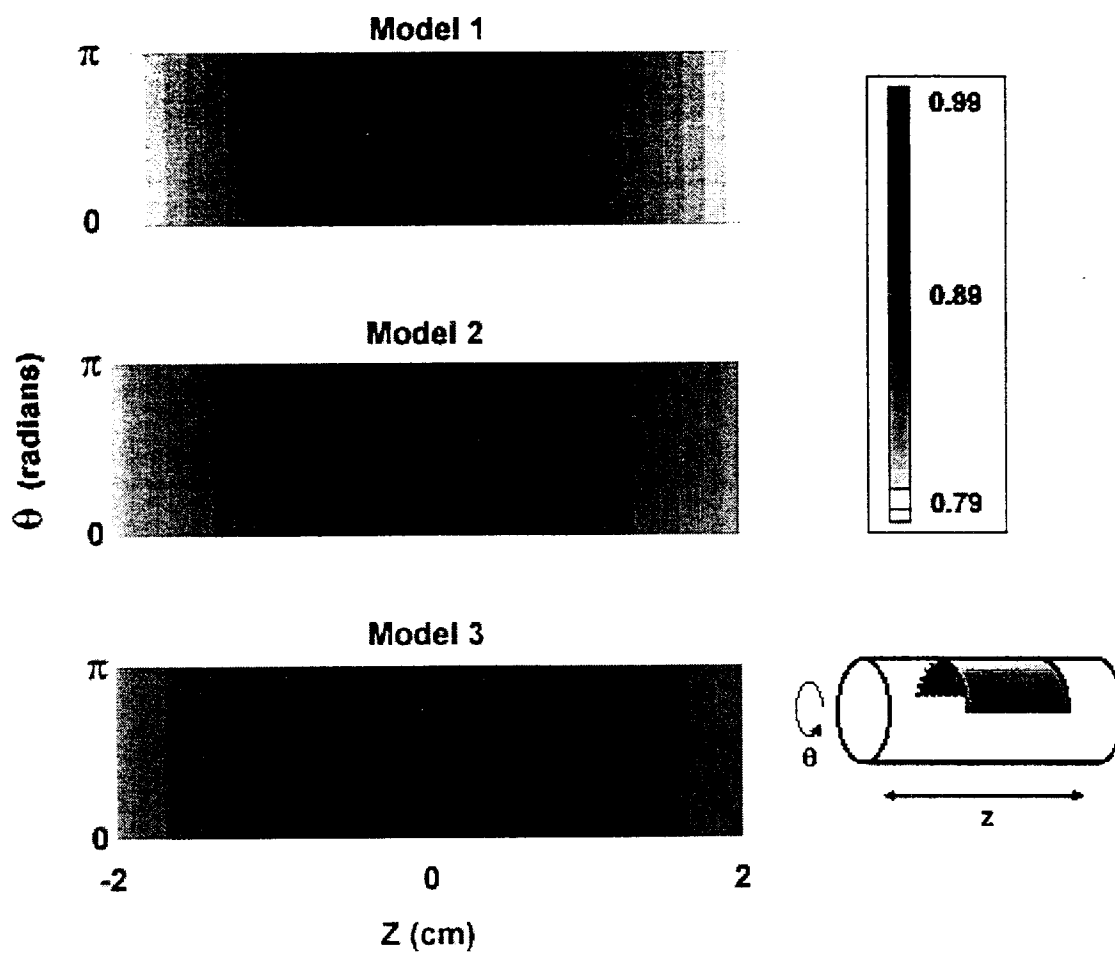


FIGURE 6.5: The contour graphs above are normalized potential maps of the cylinder surface; maps generated by each of the three forward models are displayed. These maps can be thought of as a region “unwrapped” from around the cylinder surface; a small reference diagram has been included in the bottom right hand corner of the figure.

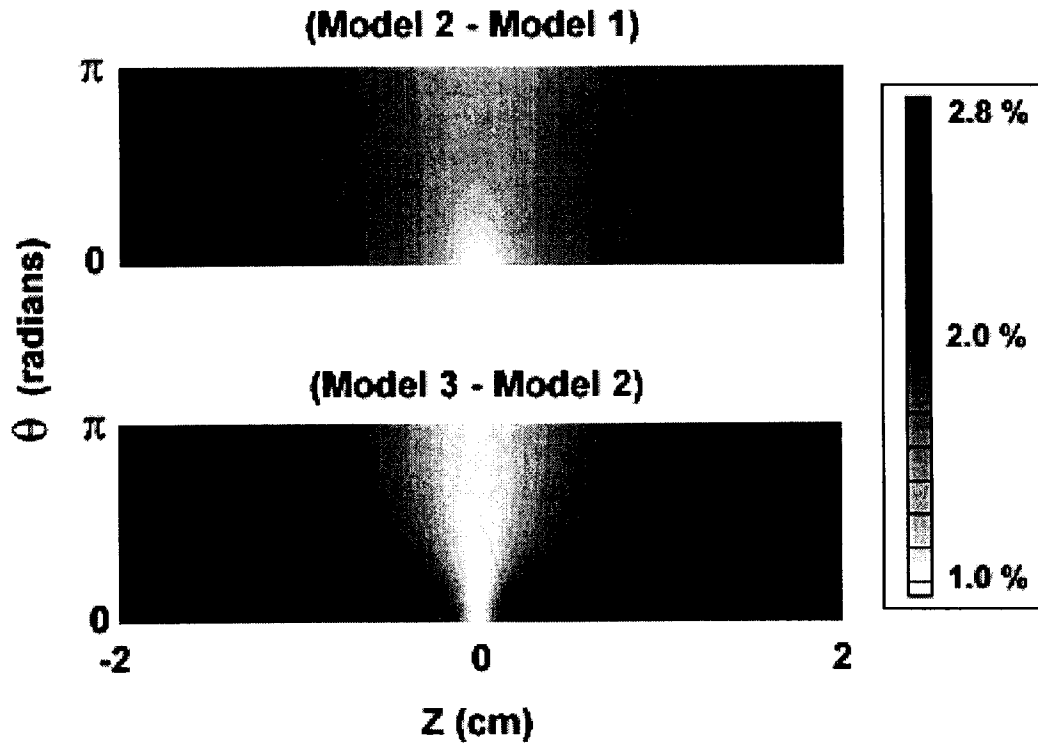


FIGURE 6.6: The contour graphs above are generated by taking the difference between two normalized surface potential maps that have been computed using the forward models. The top map reveals the difference between the first and second forward models, showing the effect of adding inhomogeneity to the model. The map on the bottom illustrates the difference between the second and third forward models, showing the effect of incorporating anisotropy into the outer cylindrical region.

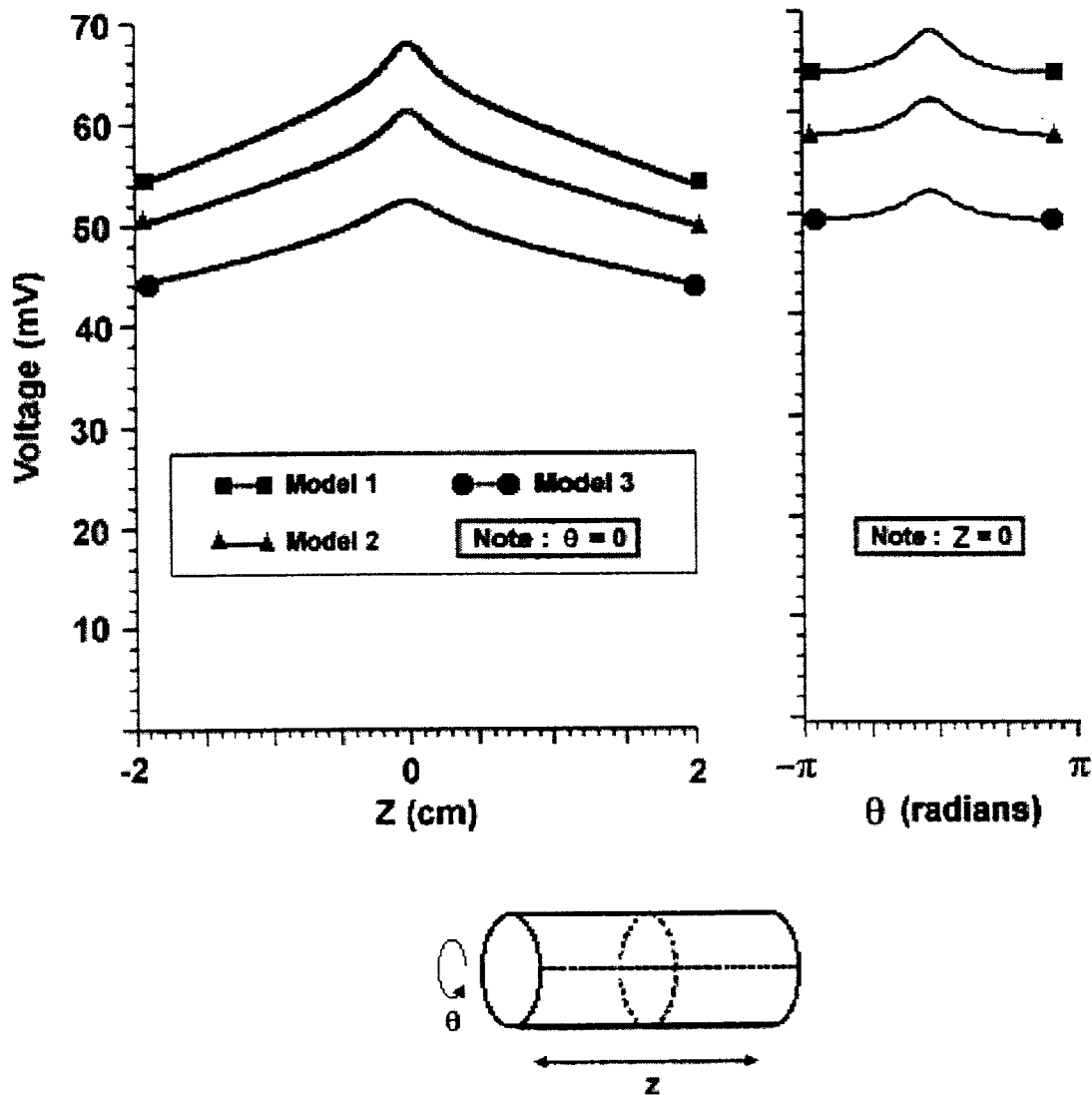


FIGURE 6.7: This figure presents a comparison of the outputs of the three models by looking at specific lines, namely $Z=0$ and $\theta=0$. These lines are denoted in the reference diagram at the bottom of the figure by the dotted lines. One key feature of the figure is the significant drop in magnitude that accompanies the addition of inhomogeneity and anisotropy. The graphs of this figure are also useful for comparing the change in surface potential profile shape; note that the shapes become smoother in the z -direction with increasing model complexity. This is also true in the θ -direction, but to a much smaller

TABLE 1		
Parameter	Value	Description
r_1	2.5mm	Inner cylindrical radius
r_2	3.5mm	Outer cylindrical radius
σ_i	0.2 S/m	Inner cylindrical conductivity
σ_i	0.2 S/m	Inner cylindrical conductivity
σ_t	0.0833 S/m	Outer cylindrical conductivity (transverse)
σ_e	0.0005 S/m	Bath conductivity
b	2.0mm	Source location (b,0,0)
ρ	3.5mm	Observation radius ($\rho = r$ for surface)
I	10 μ A	Source Strength
M	7168	One half the number of z-freq. terms
N	16	One half the number of θ -freq. terms
Z	0.2mm	Space domain sampling interval

TABLE 6.1: Parameters used in the third forward model for the source location sensitivity analysis. Note that the given 'b' value must obviously be changed to analyze model sensitivity in the ρ -direction; the given value was use for the sensitivity analysis in the θ -direction.

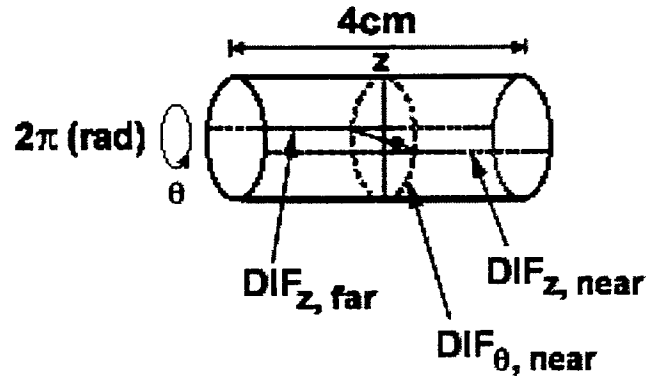


FIGURE 6.8: The diagram above illustrates the specified ranges of the parameter DIF that are used in the source location sensitivity analysis. The three DIF ranges used are:

DIF_{z, near}, which lies along $\theta = 0$ for $-2\text{cm} \leq z \leq 2\text{cm}$; the designation “near” is made because of all the lines running parallel to the z-axis on the cylinder surface, it is the line closest to the source.

DIF_{z, far}, which lies along $\theta = \pi$ for $-2\text{cm} \leq z \leq 2\text{cm}$; the designation “far” is made because of all the lines running parallel to the z-axis on the cylinder surface, it is the line furthest from the source.

DIF_{θ, far}, which lies along $z = 0$ for $-\pi \leq \theta \leq \pi$; the designation “near” is made because of all the circles on the cylinder surface, in planes perpendicular to the z-axis, it is the circle closest to the source.

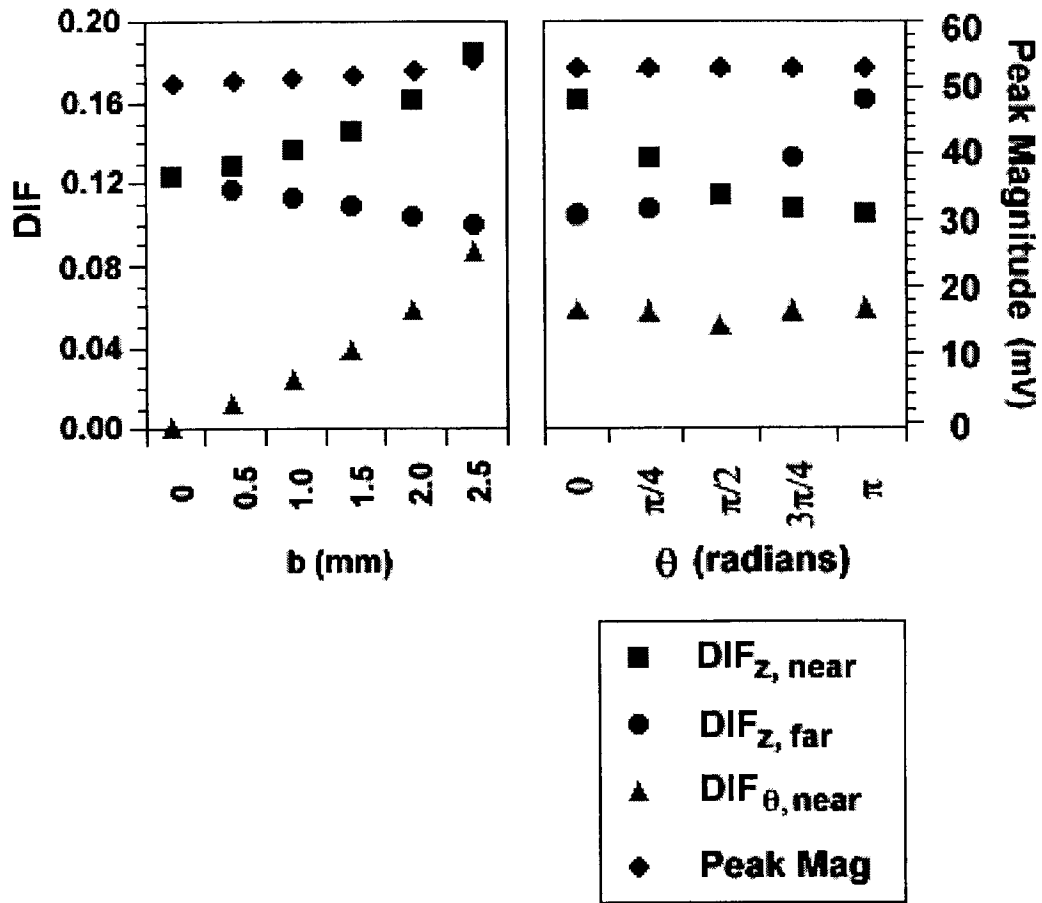


FIGURE 6.9: Values of the parameter DIF and the peak magnitude of the model output vary as the source location is changed in the ρ -direction (left plot), and in the θ -direction (right plot). Because the model output is normalized prior to calculating DIF, the highest possible value of DIF is one; however, DIF was never larger than 0.2 over the specified range.

PUBLICATIONS THIS QUARTER

Grill, W.M. (2000) Electrical activation of spinal neural circuits: application to motor-system neural prostheses. Neuromodulation 3:89-98.

OBJECTIVES FOR THE NEXT QUARTER

In the next quarter we will continue our co-localization studies to identify inhibitory spinal neurons active during micturition. Specifically, we will use immunocytochemical detection of glycine in combination with previous techniques for detection of c-Fos to identify inhibitory (glycinergic) neurons that are active during reflex micturition (express c-Fos) [Grill et al., 1998].

We will continue our studies characterizing the hindlimb motor responses to lumbar microstimulation. Our specific objective is to begin experiments using the two degree-of-freedom planar manipulator to measure the dynamic hindlimb motor responses evoked by microstimulation of the lumbar spinal cord.

LITERATURE CITED

Dapson, R.W. (1993) Fixation in the 1990s: a review of needs and accomplishments. Biotechnol. Histochem. 68:75-82.

Fox, C.H., F.B. Johnson, J. Whiting, P.P. Roller (1985) Formaldehyde fixation. J. Histochem. Cytochem. 33:845-53.

Grill, W.M., B. Wang, S. Hadziefendic, M.A. Haxhiu (1998) Identification of the spinal neural network involved in coordination of micturition in the male cat. Brain Research 796:150-160.

Jiao, Y., Z. Sun, T. Lee, F.R. Fusco, T.D. Kimble, C.A. Meade, S. Cuthbertson, A. Reiner (1999) A simple and sensitive antigen retrieval method for free-floating and slide-mounted tissue sections. J. Neurosci. Methods 93:149-162.

Morgan, J.M., H. Navabi, B. Jasani (1997) Role of calcium chelation in high-temperature antigen retrieval at different pH values. J. Pathol. 182:233-237.